Progress In Electromagnetics Research, Vol. 181, 61-72, 2024

(Received 26 November 2024, Accepted 22 December 2024, Scheduled 23 December 2024)

An Efficient Hybrid Numerical T-Matrix Approach for 3D Multiple Scattering Analysis

Haifeng Zheng[1, †], Xuyang Bai[1, 2, †], Shurun Tan[1, 2, 3, *], and Leung Tsang[4]

[1] *Zhejiang University-University of Illinois Urbana-Champaign Institute*
Zhejiang University, Haining 314400, Zhejiang, China
[2] *State Key Laboratory of Extreme Photonics and Instrumentation*
College of Information Science and Electronic Engineering, Zhejiang University, Hangzhou 310027, China
[3] *Department of Electrical and Computer Engineering, University of Illinois Urbana-Champaign, Urbana, IL 61801, USA*
[4] *Electrical Engineering and Computer Science, University of Michigan, Ann Arbor, MI 48105, USA*

ABSTRACT: In the past decades, with the increasing complexity of topological crystals, artificial electromagnetic (EM) materials, and EM environments, understanding their precise scattering behaviors and characteristis is turning more challenging. Traditional methods for modeling these properties often rely on full-wave simulations or analytical algorithms which are only applicable for regular shapes with plane wave incidences. These methods are inefficient for the design and broadband multiple scattering analysis of general 3D EM structures, as new simulations are required for each different scattering scenario and frequency, while solving a substantial number of unknown variables in each analysis. In this paper, a novel hybrid numerical scattering T-matrix extraction method applicable to scatterers of arbitrary shape and composition is developed in the context of the Foldy-Lax multiple scattering theory (F-L MST). Generalization is also made such that the F-L MST can be applied to multiple scattering problems with arbitrary incident fields. Once the T-matrix elements of individual scatterers are obtained through combining spherical wave expansion with full-wave numerical simulations of surface fields as proposed in the paper, it can be stored and reused, significantly reducing the overall computational complexity. Compared to conventional methods, this approach merely requires matrix inversions of moderate orders in a multiple scattering problem, offering notable efficiency advantages for about an order of magnitude. Meanwhile, the smooth frequency dependence of the T-matrix elements and incident field coefficients suggests the feasibility of interpolating these coefficients for broadband simulations. This proves particularly helpful in the swiftly evolving near-field techniques, and scenarios requiring extensive analysis such as broadband and Monte Carlo analysis. Numerical cases, involving multiple scatterer shapes and arrangements, are explored and compared with COMSOL full-wave simulations. The results validate the accuracy and efficiency of the proposed method, with potential to become a powerful tool for EM simulations and optimization of various wave-functional materials and in many other multiple scattering applications.

1. INTRODUCTION

Multiple scattering modeling is significant in various application scenarios not limited to topological crystals [1], artificial EM materials [2], EM information transmission analysis [3, 4], and power integrity/signal integrity (PI/SI) circuit design simulations [5–7]. In recent years, the increasing complexity of structures and the growing demand for wideband simulations have required an efficient multiple scattering approach for structures applicable to arbitrary shapes and frequencies [8, 9]. Traditional simulation modeling often relies on numerical full-wave simulations, such as finite element method [10, 11], finite difference time domain method [12, 13], and method of moment [14], which typically require dense discretization of space or surfaces, and introduce a large number of unknowns, resulting in relatively low simulation efficiency. This becomes particularly challenging when considering structures with wavelengths comparable to or smaller than the structures. Analytical methods based on spherical wave expansion offer a more efficient alternative [15]. By calculating and combining the T-matrices of individual scatterers, these methods require only a few tens of wave expansion orders without the need for complex meshing, demonstrating powerful computational efficiency [16]. Moreover, once the T-matrices of the scatterers are computed, they can be stored in a library for ongoing reuse, which will not require solving anew each time, with the ability to leverage past calculations [17]. However, existing analytical methods mostly consider regular shapes, where the T-matrix of an individual scatterer has a standardized analytical form, which is not applicable to the analysis of complex-shaped scatterers. Three well-established methods, namely the method of separation of variables (MSV) [18], the extended boundary condition method (EBCM) [19], and the point-matching method (PMM) [20], have been developed to tackle the issue of scattering by irregular particles. However, EBCM is only better suited for spherical particles, while MSV is proved to be more appropriate for Chebyshev particles [21]. Despite the potential advantages of PMM in more complex scenarios, it still does not offer a wholly satisfactory solution due to the uncertain applicability of the assumed Rayleigh hypothesis to arbitrary scatterers [20].

---

* Corresponding author: Shurun Tan (srtan@intl.zju.edu.cn).
† The co-first authors.

doi:10.2528/PIER24112606

Published by THE ELECTROMAGNETIC ACADEMY

Attempts have been made to overcome the limitations mentioned above. For example, Reference [22] derived the scattering field coefficients of the vector spherical wave functions using the far field represented by the outgoing spherical harmonic modes in the generalized transition matrix (GTM) framework [23], and obtained the T-matrix using numerical methods. Reference [24] used plane waves for excitation and obtained a T-matrix from the the far-field scattering amplitudes. Since both methods rely on the far field to obtain the T-matrix, they overlook near-field effects, which leads to inaccuracies in near-field coupling when using the T-matrix to calculate the fields. Meanwhile, Reference [25] directly determined the T-matrix of arbitrarily shaped scatterers from the impedance matrix in the method of moment (MoM) using Rao-Wilton-Glisson basis functions, which limited the approach to handle homogeneous scatterers. In the context of two-dimensional electromagnetic scattering, Reference [26] proposed an alternative method based on the transformation between cylindrical waves and plane waves. This approach addresses the issue in multiple scattering problems where the Graf addition theorem fails to provide accurate calculations when the circumcircle enclosing the scatterers overlap.

Meanwhile, with recent advances in topological photonic crystals [27, 28] and the extensive analysis of near-field effects [29–31], an efficient modeling approach for complex incident fields, including point source excitations, is highly needed. However, many T-matrix methods typically consider scenarios with plane wave excitation [17, 32], where the incidence wave coefficients are with determined analytical expressions, which cannot be directly applied to the analysis of complex excitations.

To address these deficiencies, in this paper, an efficient multiple scattering modeling approach generally applicable to structures of arbitrary shapes with arbitrary incidence waves is proposed. The proposed approach comprises two key steps. Firstly, an efficient T-matrix extraction approach for individual scatterers of arbitrary shapes is introduced. The Huygens principle as well as the wave expansion formula is utilized to relate the scattering fields coefficients with the surface fields on the enclosing surface of the scatterer which is shown in Fig. 1(a). Subsequently, the T-matrix of the scatterer can be correlated with the surface fields under each basic wave excitation. Through numerical simulations, the surface fields on the enclosing surface corresponding to each incidence can be calculated, enabling the acquiring of each element of the T-matrix. Since we establish the relationship between the T-matrix and the surface fields on the enclosing surface near the scatterer, and the solution for the surface fields employing numerical algorithms are fully applicable to scatterers of arbitrary shapes, the proposed T-matrix extraction method in this paper is versatile and can be applied to the analysis of scatterers of arbitrary shapes and non-homogeneous materials, while also can accurately represent the near-field state. Moreover, in this paper, we further consider the scattering modeling from multiple scatterers as shown in Fig. 1(b). The general applied Foldy-Lax multiple scattering theory is applied with the obtained T-matrix. It is performed by representing the excitation field of each independent scatterer as a superposition of the incident field and the scattered field from other scatterers, and subsequently constructing the coefficient equation with spherical wave expansions. Additionally, to meet the requirements of complex excitations, we derive the expression of incident field coefficients under excitation of arbitrary current distributions by combining numerical simulations. Finally, numerical examples are provided and compared with the full-wave commercial software COMSOL, corroborating the accuracy and efficiency of the proposed method.

This paper is organized as follows. In Section 2, the relation between field expansion coefficients and the surface fields on the enclosing surface is derived. And the calculation of T-matrix is discussed. In Section 3, the utilization of spherical wave functions for the derivation of the incident field of an arbitrary source is elucidated with the illustration of an infinitesimal electric dipole (i.e., a Hertzian dipole). Section 4 provides a concise introduction to the Foldy-Lax multiple scattering theorem and demonstrates its application in conjunction with the T-matrix to achieve a reduction in computing complexity. This approach is then compared with the results obtained using the COMSOL software. Finally, the conclusions are drawn in Section 5.

2. EFFICIENT EXTRACTION OF T-MATRIX FOR ARBITRARY-SHAPED SCATTERERS

2.1. T-Matrix Extraction: The Hybrid Numerical Approach

We first consider the T-matrix extraction for one individual arbitrary-shaped scatterer, as shown in Fig. 1(a) as an illustrative example. The scatterer can be of any material, or even a mixture of multiple materials. A closed surface of arbitrary shape S_1 is assumed to be situated outside the scatterer, with a normal vector $\hat{n}$ oriented outward. We denote the region inside the boundary S_1 to be V_1, while the region outside is denoted as V_0. In Fig. 1(a), O is the center of the spherical wave expansion in the T-matrix formulation, and S_v is the smallest spherical surface centered at O that encloses the boundary S_1. The region outside S_v forms the validity domain of the T-matrix derived from the hybrid method to be discussed.

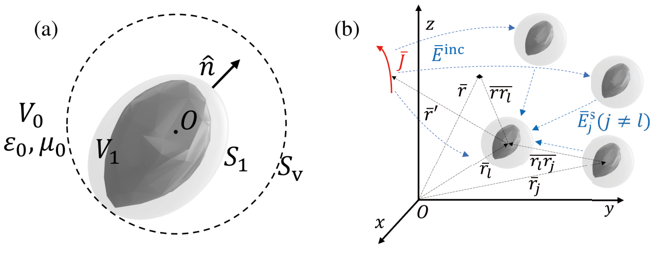

FIGURE 1. (a) T-matrix extraction for arbitrary-shaped scatterer. (b) The application of T-matrix in multiple scattering problems.

The total fields, incident fields, and surface fields in space satisfy the Huygens' principle, assuming the $\exp(-i\omega t)$ convention,

$$\begin{cases} \overline{E}\left(\overline{r}\right) & \text{if } \overline{r} \in V_0 \\ 0 & \text{if } \overline{r} \in V_1 \end{cases}$$

$$= \overline{E}^{inc}(\overline{r}) + \int_{S_1} \mathrm{d}S' \left\{ \overline{\overline{G}}_o(\overline{r}, \overline{r}') \cdot \hat{n} \times i\omega\mu_0 \overline{H}(\overline{r}') \right.$$

$$\left. + \nabla' \times \overline{\overline{G}}_o(\overline{r}, \overline{r}') \cdot \hat{n} \times \overline{E}(\overline{r}') \right\} \tag{1}$$

where $\overline{E}$, $\overline{E}^{inc}$, and $\overline{H}$ denote the total electric field, incident field (excitation field), and the total magnetic field, respectively. $\overline{r}$ and $\overline{r}'$ represent the observation point and source point, respectively. $\overline{\overline{G}}_0(\cdot)$ is the free space dyadic Green's function, and ω denotes the angular frequency of the wave in free space. The second term on the right-hand side of Eq. (1) represents the scattered field $\overline{E}^s$.

For a single scatterer, the incident fields and the scattered fields in region V_0 can be expanded into spherical wave of each order, represented as,

$$\overline{E}^{inc}(\overline{r}) = \overline{E}^{ex}(\overline{r}) = \sum_{n,m} \left\{ a_{mn}^{e(M)} Rg\overline{M}_{mn}(kr, \theta, \phi) \right.$$

$$\left. + a_{mn}^{e(N)} Rg\overline{N}_{mn}(kr, \theta, \phi) \right\} \tag{2}$$

$$\overline{E}^s(\overline{r}) = \sum_{n,m} \left\{ a_{mn}^{s(M)} \overline{M}_{mn}(kr, \theta, \phi) \right.$$

$$\left. + a_{mn}^{s(N)} \overline{N}_{mn}(kr, \theta, \phi) \right\} \tag{3}$$

where $a_{mn}^{e(M)}$ and $a_{mn}^{e(N)}$ are defined as the incident field coefficients, while $a_{mn}^{s(M)}$ and $a_{mn}^{s(N)}$ are defined as the scattered field coefficients. The value of the order n should be a positive integer. For a specific order $n = n_0$, the value of m ranges from $-n_0$ to n_0 as an integer. For example, when $n = 1$, all the (m, n) values can be listed as $(-1, 1)$, $(0, 1)$, and $(1, 1)$. When $n = 2$, they will be $(-2, 2)$, $(-1, 2)$, $(0, 2)$, $(1, 2)$, and $(2, 2)$. $Rg\overline{M}_{mn}$, $Rg\overline{N}_{mn}$, $\overline{M}_{mn}$ and $\overline{N}_{mn}$ denote the basic spherical waves (c.f. page 27 of [33]). In Eq. (2), since the incident field is assumed to be finite at the center of scatterer, the regular vector spherical waves with prefix Rg is utilized. The scattering fields described as Eq. (3), will be a linear combination of outgoing spherical waves outside scatterer, therefore they are expanded without the prefix Rg. k is the wave number in region V_0, and (r, θ, ϕ) denote the spherical coordinates of the observation point $\overline{r}$. Moreover, the free space dyadic Green's function can be also expanded as basic spherical waves (c.f. page 60 of [33]) as,

$$\overline{\overline{G}}_o(\overline{r}, \overline{r}') = ik \sum_{n,m} (-1)^m$$

$$\times \begin{cases} \overline{M}_{-mn}(kr, \theta, \phi) Rg\overline{M}_{mn}(kr', \theta', \phi') \\ + \overline{N}_{-mn}(kr, \theta, \phi) Rg\overline{N}_{mn}(kr', \theta', \phi') & \text{for } r > r' \\ Rg\overline{M}_{-mn}(kr, \theta, \phi) \overline{M}_{mn}(kr', \theta', \phi') \\ + Rg\overline{N}_{-mn}(kr, \theta, \phi) \overline{N}_{mn}(kr', \theta', \phi') & \text{for } r' > r \end{cases} \tag{4}$$

Substituting Eq. (3), and Eq. (4) with condition that $r > r'$, into Eq. (1), the relations between the scattered field coefficient and the surface field on the enclosing surface can be obtained,

$$\begin{bmatrix} a_{mn}^{s(M)} \\ a_{mn}^{s(N)} \end{bmatrix} = ik(-1)^m \int_{S_1} \mathrm{d}S' \hat{n} \times i\omega\mu \overline{H}(\overline{r}')$$

$$\cdot \begin{bmatrix} Rg\overline{M}_{-mn}(kr', \theta', \phi') \\ Rg\overline{N}_{-mn}(kr', \theta', \phi') \end{bmatrix} + ik^2(-1)^m \int_{S_1} \mathrm{d}S' \hat{n} \times \overline{E}(\overline{r}')$$

$$\cdot \begin{bmatrix} Rg\overline{N}_{-mn}(kr', \theta', \phi') \\ Rg\overline{M}_{-mn}(kr', \theta', \phi') \end{bmatrix} \tag{5}$$

The T-matrix is defined as the matrix linking the incidence field coefficients and the scattered field coefficients,

$$\overline{a}^s = \overline{\overline{T}}\,\overline{a}^e. \tag{6}$$

Considering that each (m, n)th order spherical wave has two different spherical wave components represented as M and N as shown in Eqs. (2) and (3), we arrange the coefficients in the matrix as,

$$\begin{bmatrix} \overline{a}^{s(M)} \\ \overline{a}^{s(N)} \end{bmatrix} = \begin{bmatrix} \overline{\overline{T}}^{(11)} & \overline{\overline{T}}^{(12)} \\ \overline{\overline{T}}^{(21)} & \overline{\overline{T}}^{(22)} \end{bmatrix} \begin{bmatrix} \overline{a}^{e(M)} \\ \overline{a}^{e(N)} \end{bmatrix} = \overline{\overline{T}} \begin{bmatrix} \overline{a}^{e(M)} \\ \overline{a}^{e(N)} \end{bmatrix} \tag{7}$$

which also aligns with the representation of the scattered field coefficient as shown in Eq. (5). To express the field coefficients in a more concise manner and arrange them into column vectors, let's define the truncation number of n to be $N_{\max}$. We recall that when n takes on a specific positive integer value n_0, m ranges from $-n_0$ to n_0. Therefore, when n is truncated by $N_{\max}$ (n from 1 to $N_{\max}$), the total number of (mn) terms is given by $L_{\max} = N_{\max}(N_{\max} + 2)$. And $\overline{\overline{T}}^{(11)}$, $\overline{\overline{T}}^{(12)}$, $\overline{\overline{T}}^{(21)}$, and $\overline{\overline{T}}^{(22)}$ will be matrices with size $L_{\max} \times L_{\max}$. A combined index l can be then used to represent the two indices n and m as $l = n(n + 1) + m$. The column vector in Eq. (7) is now arranged based on the index l.

To obtain the T-matrix, we employ a strategy scanning the incident wave order by order for each elementary spherical waves. Specifically, in each case, we set one element of the excitation field coefficients $\overline{a}^e$ to 1 while the remaining elements are set to 0. As an example, let's consider the excitation by the ith spherical wave. In this case, the element in the ith row of $\overline{a}^e$ is set to 1, while the rest are set to 0, forming the excitation field. Eq. (6) in this case becomes $\overline{a}^s = \overline{T}_i a_i^e = \overline{T}_i$, i.e., the ith column of the T-matrix. The corresponding surface fields under such excitation field can be next calculated from numerical simulations. For calculating the surface fields, in this paper, the commercial software COMSOL is utilized. COMSOL has the flexibility to apply user-defined excitation fields in a scattering problem. Specifically, the excitation fields can be coded in Matlab and then being called by COMSOL [34, 35]. By substituting these computed fields into Eq. (5), the coefficients of the scattered field corresponding to this excitation can be next obtained. As a_i^e is specified as 1, the resulting vector of scattered field coefficients will be equivalent to the ith column of

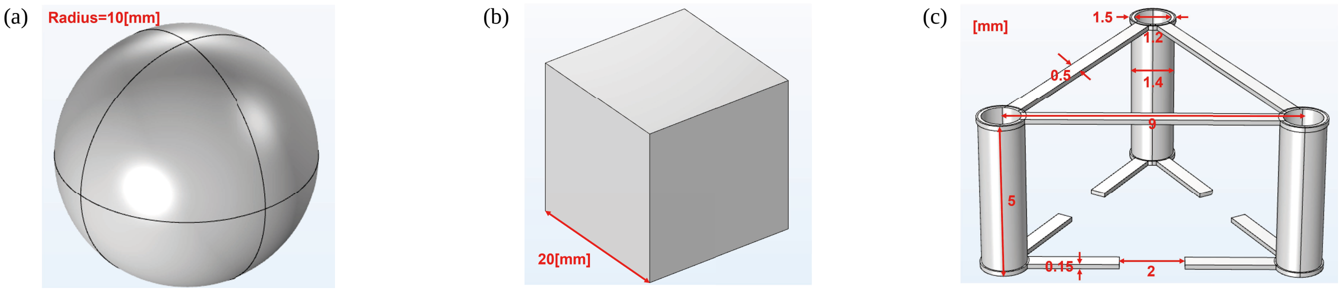

FIGURE 2. Illustrations to the exampled structures. (a) A sphere with a radius of 10 mm and a relative permittivity of 5. (b) A cube with a side length of 20 mm and a relative permittivity of 5. (c) A complex structure composed of copper with a conductivity of $5.998 \times 10^7\,\mathrm{S \cdot m^{-1}}$.

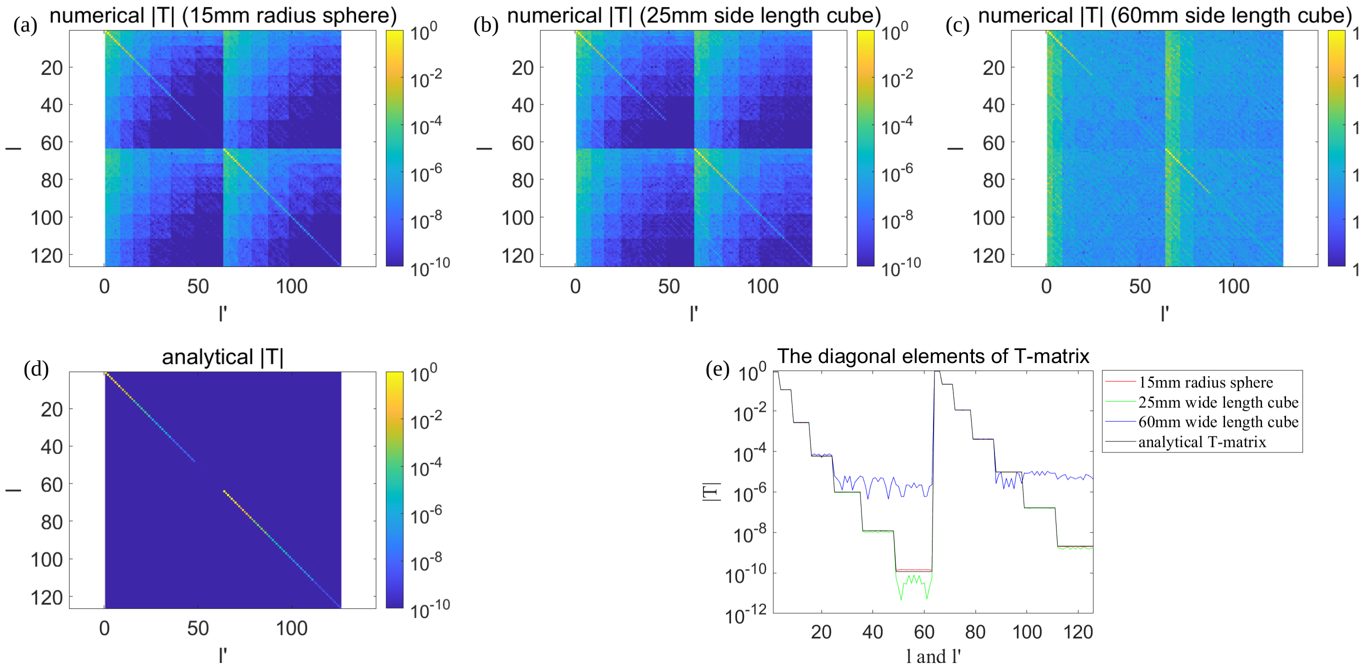

FIGURE 3. The T-matrix of a sphere whose center is at the center of a spherical wave expansion is. (a) T-matrix of a sphere extracted on a 15 mm radius sphere as a enclosing surface. (b) T-matrix of a sphere extracted on a 25 mm side length cube as a enclosing surface. (c) T-matrix of a sphere extracted on a 60 mm side length cube as a enclosing surface. (d) Analytical T-matrix of a sphere. (e) Comparison of T-matrices derived from distinct enclosed surfaces with analytic T-matrix in the diagonal elements.

the T-matrix. By repeating this procedure for each excitation (i ranging from 1 to $2L_{\max}$), we can ultimately solve for and obtain the complete T-matrix. Due to the numerical algorithms being shape-independent, it is evident that the proposed method can be readily applied to obtain the T-matrix of scatterers with arbitrary shapes.

For a single scatterer scattering problem, once the T-matrix of the scatterer is obtained, the scattered field can be readily derived with Eq. (7) for a specific excitation field. The coefficients of the excitation field are typically readily obtained through straightforward deductions (c.f. page 86 of [33]) for plane waves, and the coefficients are derived for arbitrary sources in Section 3.

2.2. Numerical Validation of the Extracted T-Matrix

To validate the proposed method, we conducted experiments using three example structures as depicted in Fig. 2. All experiments were conducted within a vacuum environment. Fig. 2(a) shows a sphere with a radius of 10 mm and a relative permittivity of 5. Fig. 2(b) illustrates a cube with a side length of 20 mm, also with a relative permittivity of 5. Fig. 2(c) portrays a more complex structure constructed using copper material, which exhibits a conductivity of $5.998 \times 10^7\,\mathrm{S \cdot m^{-1}}$. The T-matrix elements reported below are computed at 7.5 GHz for the sphere and cube, while those for the complex structure are calculated at 5 GHz.

We first consider the T-matrix of the single sphere scatterer, i.e., Fig. 2(a). The maximum order of spherical wave expansion applied is $N_{\max} = 7$ ($L_{\max} = 63$). The enclosing surfaces (S_1) used to solve for the T-matrix in Eq. (5) consist of a sphere with a radius of 15 mm, a cube with a side length of 25 mm, and a cube with a side length of 60 mm, respectively. We compare the obtained T-matrix with its analytical solutions[1] as shown in Figs. 3(a)–(d). The detailed comparison between the diago-

---

[1] The T-matrix for a dielectric sphere has an analytical solution (c.f. page 98 of [33]).

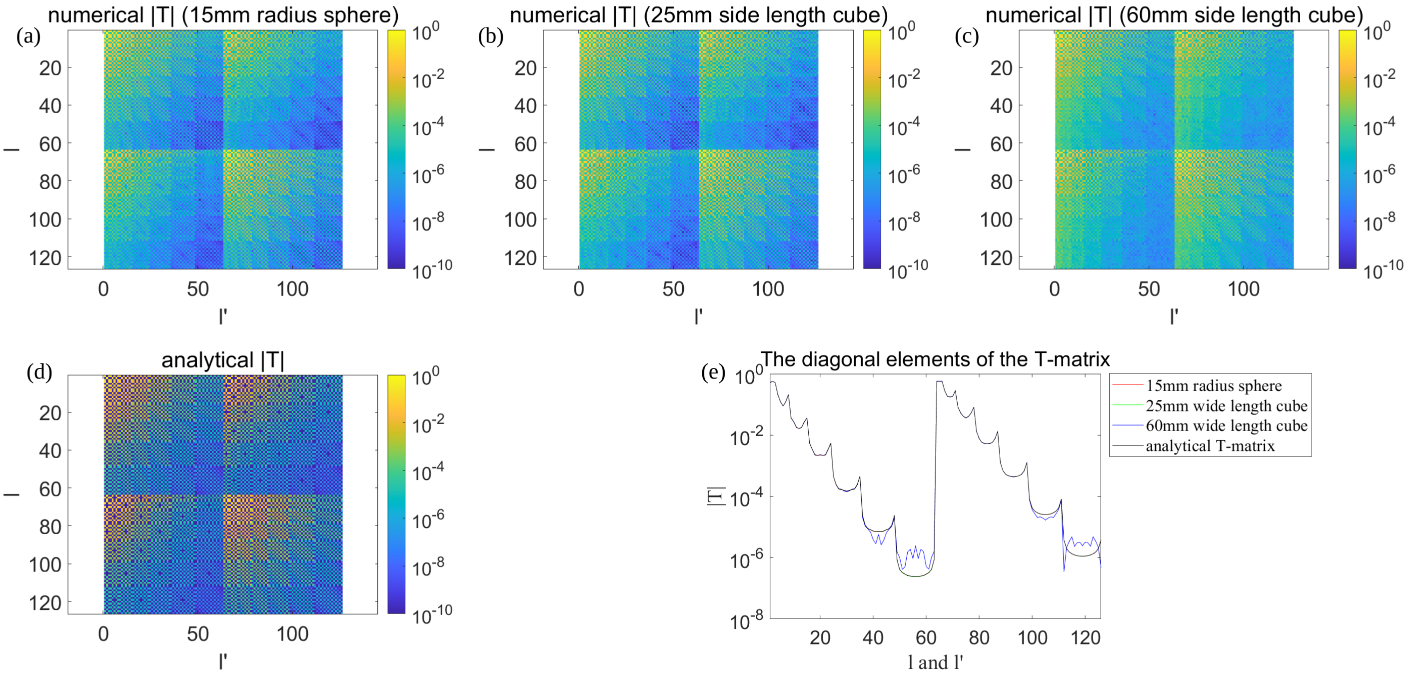

FIGURE 4. The T-matrix of a sphere whose center is situated at a distance of 0.01 m in the positive x-direction from the center of the spherical wave expansion. (a) T-matrix of a sphere extracted on a 15 mm radius sphere as a enclosing surface. (b) T-matrix of a sphere extracted on a 25 mm side length cube as a enclosing surface. (c) T-matrix of a sphere extracted on a 60 mm side length cube as a enclosing surface. (d) Analytical T-matrix of a sphere. (e) Comparison of T-matrices derived from distinct enclosed surfaces with analytic T-matrix in the diagonal elements.

nal elements of the obtained and analytical T-matrices, are also depicted in Fig. 3(e). It is evident that the obtained T-matrix closely matches the analytical solution for each case, while the T-matrix obtained from the spherically enclosed surface performed the best.

These experimental results demonstrate that using a circumsphere as the enclosing surface for calculating the T-matrix is not a necessary condition. Satisfactory results were also achieved using a circum-cube in this specific example. Meanwhile, as evident from Fig. 3(e), the distance between the enclosing surface and the scatterer will affect the quality of the extracted T-matrix, particularly for higher-order elements. A closer proximity will generally result in more accurate results.

In a further experiment, the sphere center was changed to be displaced at $+0.01$ m (equivalent to one radius) along x-axis, and the T-matrix was recalculated using the same enclosing surfaces as depicted in Fig. 3. In these cases, there is a displacement between the enclosing surfaces and the center of the scatterer. The results are presented in Fig. 4. The analytical T-matrix solution in these cases is obtained by utilizing the T-matrix from Fig. 3(d) in conjunction with the addition theorem [36]. The results obtained in this experiment confirmed conclusions observed in Fig. 3. Moreover, when comparing the recalculated T-matrix with those in Fig. 3, we also discover that even a minor displacement of the scatterer center can lead to a significant alteration in the T-matrix elements.

Furthermore, we have extracted the T-matrix for the other two scatterers, and the results are presented in Fig. 5. The shape and size of the enclosing surface used for T-matrix extraction are also indicated in the plot titles. Same conclusions can be obtained in the presented results. As the distance between the enclosing surface and the scatterer increases, the higher-order elements of the T-matrix become less accurate.

We further conducted an examination of the broadband properties of the T-matrix elements. Fig. 6 illustrates the real and imaginary parts of several representative T-matrix elements as a function of frequency for the sphere and the complex structure example, respectively. The frequency of the sphere begins at 6.6 GHz and increases to 15 GHz (with electrical size ranging from 0.44 to 1), while the complex structure begins at 4.4 GHz and rises to 15 GHz (with electrical size ranging from 0.23 to 0.8). Results indicate a smooth change of both real and imaginary parts of the T-matrix elements in log-scale with frequency. This is checked to be representative for all substantial T-matrix elements not polluted by numerical noise.

3. SPHERICAL WAVE EXPANSION OF EXCITATION FIELDS

Consider the case when a group of scatterers is excited by an incident field due to an arbitrary current distribution $\overline{J}(\overline{r}')$, c.f. Fig. 1(b). To apply the T-matrix analysis, the incident fields need to be represented in terms of spherical waves centered around each scatterer as indicated in Eq. (2). To facilitate this conversion, we invoke the free-space dyadic Green's function, c.f. Eq. (4) for $r' > r$ in [37]

$$\overline{E}^{inc}(\overline{r}) = i\omega\mu_0 \int \mathrm{d}\overline{r}'\, \overline{\overline{G}}_0(\overline{r},\overline{r}') \cdot \overline{J}(\overline{r}') \qquad (8)$$

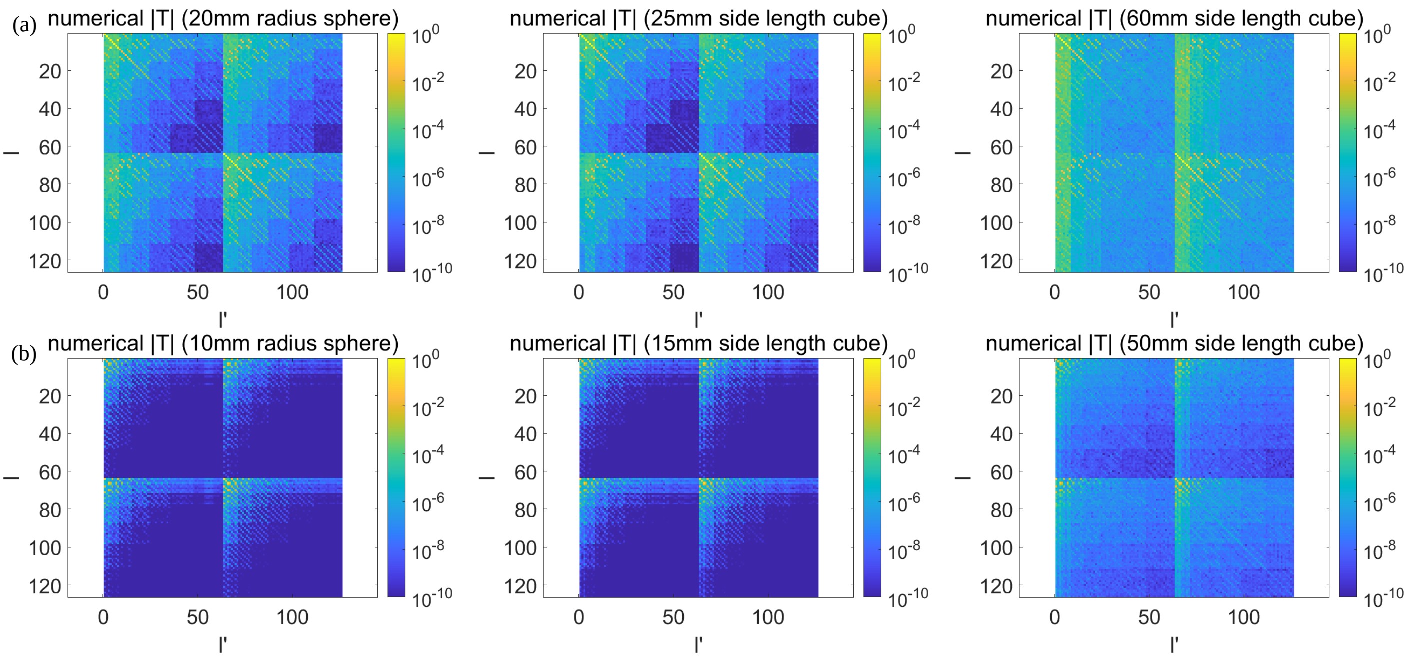

FIGURE 5. T-matrix for different examples. (a) T-matrix of cube. (b) T-matrix of complex structure.

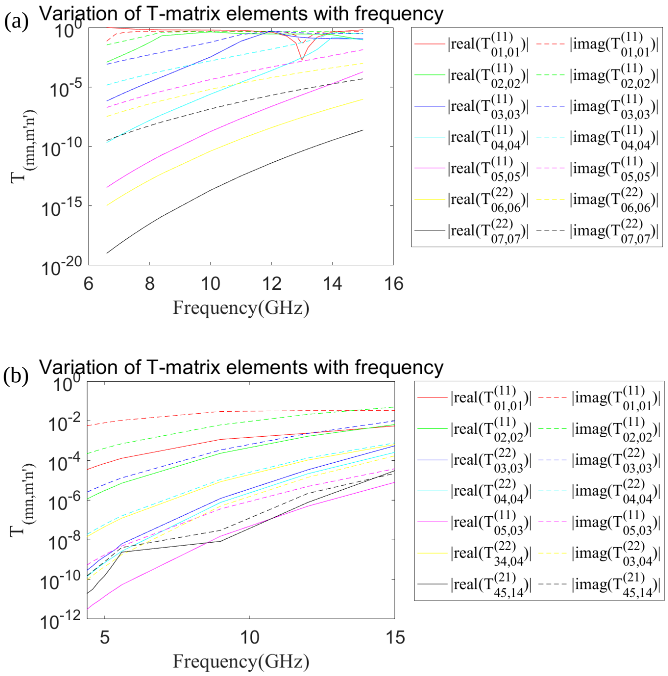

FIGURE 6. The variation of the real and imaginary parts of the T-matrix elements as a function of frequency. (a) The T-matrix elements of a sphere. (b) The T-matrix elements of a complex structure.

and matching the result with Eq. (2) to obtain the incident wave coefficients

$$\begin{bmatrix} a^{e(M)}_{mn} \\ a^{e(N)}_{mn} \end{bmatrix} = ik(-1)^m \int \mathrm{d}\overline{r}' \begin{bmatrix} \overline{M}_{-mn}\left(kr', \theta', \phi'\right) \\ \overline{N}_{-mn}\left(kr', \theta', \phi'\right) \end{bmatrix} \cdot iw\mu_0 \overline{J}(\overline{r}') \tag{9}$$

where the integration can be efficiently carried out numerically. Note in Eq. (9) that the primed coordinates (r', θ', ϕ') are referred to the scatterer center $\overline{r}_l$ and the resulting incident field expansion coefficients are linked to a specific scatterer.

Specifically, the radiation from a Hertzian dipole with moment $Il\hat{z}$ located at $\overline{r}'$ is converted to spherical waves centered at origin with coefficients

$$\begin{bmatrix} a^{(M)}_{mn} \\ a^{(N)}_{mn} \end{bmatrix} = ik(-1)^m \begin{bmatrix} \overline{M}_{-mn}\left(kr', \theta', \phi'\right) \\ \overline{N}_{-mn}\left(kr', \theta', \phi'\right) \end{bmatrix} \cdot iw\mu_0 Il\hat{z} \tag{10}$$

To demonstrate the efficacy of the proposed method, we provide a numerical example as depicted in Fig. 7, which assumes a scatterer centered at the origin for the wave conversion. This figure illustrates the behavior of the excited electric field along x-axis for a $\hat{z}$-directed Hertzian dipole with a moment of 1×10^{-5} A · m, at three different locations: $(-0.06, 0, 0)$, $(-0.10, 0, 0)$, and $(-0.15, 0, 0)$ m. Fig. 7(b) reveals the discrepancy between the electric field determined by spherical wave expansion and the one computed analytically. The results demonstrate that a higher order of the spherical wave employed leads to a more accurate excited field representation. Meanwhile, for the Hertzian dipoles, it is also noted that the accuracy of the numerical electric field up to the same expansion order enhances as the dipole progressively distances from the origin, an intrinsic property of the addition theorem.

The broadband properties of the incident field coefficients are also examined, and analogous properties to those of the T-matrix elements are identified. Fig. 8 shows several representative incident field coefficients of a Hertzian dipole with dipole moments of 1×10^{-5} A · m located at $(-0.10, 0, 0)$ meters. Both the modulus and the phase angles vary smoothly with frequency. This is again checked to be representative for all wave coefficients with substantial values not polluted by noise.

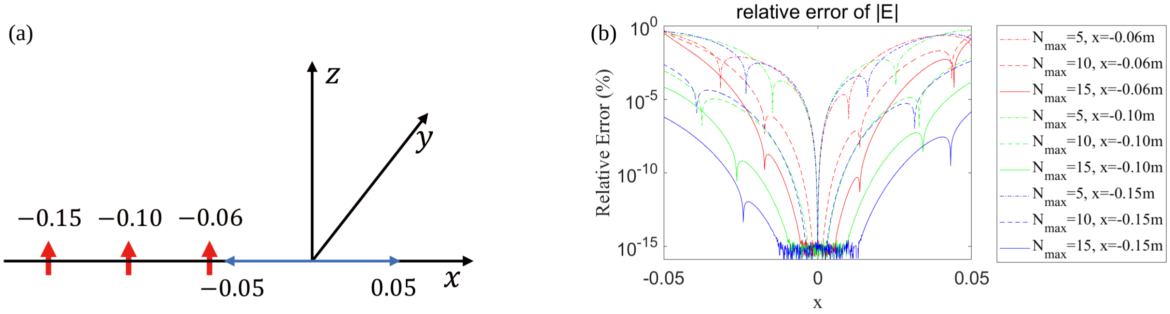

FIGURE 7. The electric fields of Hertzian dipoles located at different coordinates with dipole moments of 1×10^{-5} A · m are reduced using spherical wavefunctions of different orders, and the obtained fields are compared with the analytical ones. (a) The Hertzian dipoles are situated on the x-axis, with coordinates of $(-0.06,0,0)$, $(-0.10,0,0)$, and $(-0.15,0,0)$ meters. The calculated electric field extends over a line segment from $(-0.05,0,0)$ meters to $(0.05,0,0)$ meters. (b) The relative error of the electric field was reduced by Hertzian dipoles at different locations with spherical wave functions of varying orders in comparison to the analytical solution.

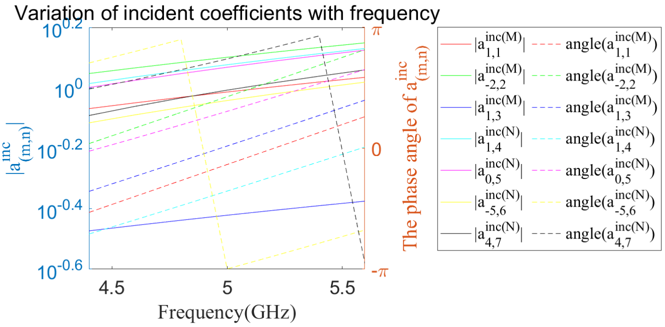

FIGURE 8. The variation of incident coefficients as a function of frequency.

4. MULTIPLE SCATTERING ANALYSIS USING THE NUMERICALLY EXTRACTED T-MATRIX

4.1. The Foldy-Lax Multiple Scattering Formulation

In this subsection, we summarize the key relations in the Foldy-Lax multiple scattering theory for the sake of completeness. In the context of the multiple scattering problem as displayed in Fig. 1(b), each scatterer is subject to the impact of the incident wave and the multiple scattered waves originating from all other objects. As a consequence, the excitation fields of each scatterer can be represented as the sum of the incident fields and the scattered fields from all other scatterers,

$$\overline{\psi}_l^{ex} = \overline{\psi}^{inc} + \sum_{\substack{j=1\\ j\neq l}}^{N_s} \overline{\psi}_j^{s} \tag{11}$$

where $\overline{\psi}_l^{ex}$ represents the excitation field on the lth scatterer; $\overline{\psi}^{inc}$ represents the incident field; and $\overline{\psi}_j^{s}$ is the scattered field from the jth scatterer. N_s denotes the number of scatterers.

The total field can be represented as the sum of the incident fields and the scattered fields from all individual scatterers,

$$\overline{\psi} = \overline{\psi}^{inc} + \sum_{j=1}^{N_s} \overline{\psi}_j^{s}, \tag{12}$$

We rewrite the expressions of Eq. (2) and Eq. (3) into the following forms:

$$\begin{aligned}\overline{E}_l^{ex}(\overline{r}) &= \sum_{n,m}\Big\{a_{mn}^{e(M)(l)} Rg\overline{M}_{mn}(k\overline{rr_l})\\ &\quad + a_{mn}^{e(N)(l)} Rg\overline{N}_{mn}(k\overline{rr_l})\Big\} \qquad (13)\\ \overline{E}_l^{s}(\overline{r}) &= \sum_{n,m}\sum_{\nu,\mu}\Big\{(a_{\mu\nu}^{e(M)(l)} T_{mn\mu\nu}^{(11)(l)}\\ &\quad + a_{\mu\nu}^{e(N)(l)} T_{mn\mu\nu}^{(12)(l)})\overline{M}_{mn}(k\overline{rr_l})\\ &\quad + (a_{\mu\nu}^{e(M)(l)} T_{mn\mu\nu}^{(21)(l)}\\ &\quad + a_{\mu\nu}^{e(N)(l)} T_{mn\mu\nu}^{(22)(l)})\overline{N}_{mn}(k\overline{rr_l})\Big\} \qquad (14)\end{aligned}$$

where the coordinates within the vector spherical waves are changed to be relative to the center of the lth scatterer, reflected in term $\overline{rr_l} = \overline{r} - \overline{r}_l$. $T_{mn\mu\nu}^{(11)(l)}$, $T_{mn\mu\nu}^{(12)(l)}$, $T_{mn\mu\nu}^{(21)(l)}$, $T_{mn\mu\nu}^{(22)(l)}$ represent the T-matrix elements of the lth scatterer, which are combined into the block T-matrix as expressed in Eq. (7).

When dealing with multiple scatterer scattering problems as displayed in Fig. 1(b), it is noted that the position of the scatterer's center is not always at the origin, requiring a wave transformation. Based on the addition theorem [36], the transformation relations of the basic spherical waves represented in two coordinates linked by a translation of the origin $\overline{r}_o = \overline{r} - \overline{r}'$ can be expressed as follows, c.f. Fig. 9,

$$Rg\overline{M}_{\mu\nu}(k\overline{r}) = \sum_{n,m}\Big\{RgA_{mn\mu\nu}(k\overline{r}_0) Rg\overline{M}_{mn}(k\overline{r}')$$

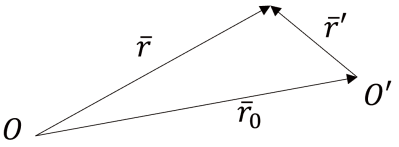

FIGURE 9. Additional theorem.

$$+RgB_{mn\mu\nu}(k\overline{r}_0)Rg\overline{N}_{mn}(k\overline{r}^{'})\Big\} \quad (15)$$

$$Rg\overline{N}_{\mu\nu}(k\overline{r}) = \sum_{n,m}\Big\{RgB_{mn\mu\nu}(k\overline{r}_0)Rg\overline{M}_{mn}(k\overline{r}^{'})$$

$$+RgA_{mn\mu\nu}(k\overline{r}_0)Rg\overline{N}_{mn}(k\overline{r}^{'})\Big\} \quad (16)$$

$$\overline{M}_{\mu\nu}(k\overline{r}) = \sum_{n,m}\Big\{A_{mn\mu\nu}(k\overline{r}_0)Rg\overline{M}_{mn}(k\overline{r}^{'})$$

$$+B_{mn\mu\nu}(k\overline{r}_0)Rg\overline{N}_{mn}(k\overline{r}^{'})\Big\} \quad (17)$$

$$\overline{N}_{\mu\nu}(k\overline{r}) = \sum_{n,m}\Big\{B_{mn\mu\nu}(k\overline{r}_0)Rg\overline{M}_{mn}(k\overline{r}^{'})$$

$$+A_{mn\mu\nu}(k\overline{r}_0)Rg\overline{N}_{mn}(k\overline{r}^{'})\Big\} \quad (18)$$

where $RgA_{mn\mu\nu}$, $RgB_{mn\mu\nu}$, $A_{mn\mu\nu}$, $B_{mn\mu\nu}$ represent the spherical wave transformations between two coordinates, whose specific definitions and calculations are reported in [38]. The coefficients that were originally obtained by expanding the wave around the origin O are now expanded around the new center O' as illustrated in Fig. 9.

In multiple scattering scenarios with N_s scatterers, subscribing Eqs. (12)–(18) to Eq. (11), the excitation field for the lth scatterer can be further derived as,

$$\sum_{n,m}\Big\{a_{mn}^{e(M)(l)}Rg\overline{M}_{mn}(k\overline{rr_l}) + a_{mn}^{e(N)(l)}Rg\overline{N}_{mn}(k\overline{rr_l})\Big\}$$

$$= \sum_{\nu,\mu}\sum_{n,m}\Big\{a_{\mu\nu}^{\text{inc}(M)}[RgA_{mn\mu\nu}(k\overline{r}_l)Rg\overline{M}_{mn}(k\overline{rr_l})$$

$$+RgB_{mn\mu\nu}(k\overline{r}_l)Rg\overline{N}_{mn}(k\overline{rr_l})]$$

$$+a_{\mu\nu}^{\text{inc}(N)}[RgB_{mn\mu\nu}(k\overline{r}_l)Rg\overline{M}_{mn}(k\overline{rr_l})$$

$$+RgA_{mn\mu\nu}(k\overline{r}_l)Rg\overline{N}_{mn}(k\overline{rr_l})]\Big\}$$

$$+\sum_{j=1,j\neq l}^{N_s}\sum_{\nu,\mu}\sum_{n',m'}\sum_{n,m}$$

$$\Big\{(a_{\mu\nu}^{e(M)(j)}T_{m'n'\mu\nu}^{(11)(j)} + a_{\mu\nu}^{e(N)(j)}T_{m'n'\mu\nu}^{(12)(j)})$$

$$\cdot[A_{mnm'n'}(k\overline{r_lr_j})Rg\overline{M}_{mn}(k\overline{rr_l})$$
$$+B_{mnm'n'}(k\overline{r_lr_j})Rg\overline{N}_{mn}(k\overline{rr_l})]$$

$$+(a_{\mu\nu}^{e(M)(j)}T_{m'n'\mu\nu}^{(21)(j)} + a_{\mu\nu}^{e(N)(j)}T_{m'n'\mu\nu}^{(22)(j)})$$

$$\cdot[B_{mnm'n'}(k\overline{r_lr_j})Rg\overline{M}_{mn}(k\overline{rr_l})+$$
$$A_{mnm'n'}(k\overline{r_lr_j})Rg\overline{N}_{mn}(k\overline{rr_l})]\Big\} \quad (19)$$

By balancing the related coefficients, it can be further simplified in a matrix form,

$$\overline{a}^{e(l)} = Rg\overline{\overline{\sigma}}(k\overline{r_l})\cdot\overline{a}^{\text{inc}} + \sum_{j=1,\,j\neq l}^{N_s}\overline{\overline{\sigma}}(k\overline{r_lr_j})\cdot\overline{\overline{T}}^{(j)}\cdot\overline{a}^{e(j)} \quad (20)$$

where $\overline{a}^{e(l)}$ denotes the coefficient vector of the excitation field on the lth scatterer, and $\overline{\overline{T}}^{(j)}$ represents the T-matrix of the jth scatterer. The translation matrix $\overline{\overline{\sigma}}(k\overline{r})$ is a $2L_{\max}\times 2L_{\max}$ matrix, detailed with block matrics as,

$$\overline{\overline{\sigma}}(k\overline{r}) = \begin{bmatrix}\overline{\overline{A}}(k\overline{r}) & \overline{\overline{B}}(k\overline{r})\\ \overline{\overline{B}}(k\overline{r}) & \overline{\overline{A}}(k\overline{r})\end{bmatrix} \quad (21)$$

The matrix elements $\overline{\overline{A}}(k\overline{r})$ and $\overline{\overline{B}}(k\overline{r})$ are composed of the elements $A_{mn\mu\nu}(k\overline{r})$ and $B_{mn\mu\nu}(k\overline{r})$ from the addition theorems in Eq. (17) and Eq. (18). These elements are arranged based on the indices determined by m, n and μ, ν, similar to how it is used in T-matrix Eq. (7), and the matrices are of dimension $L_{\max}\times L_{\max}$. The same relation holds for $Rg\overline{\overline{\sigma}}(k\overline{r})$, for which the block matrices $\overline{\overline{A}}(k\overline{r})$ and $\overline{\overline{B}}(k\overline{r})$ are changed to $Rg\overline{\overline{A}}(k\overline{r})$ and $Rg\overline{\overline{B}}(k\overline{r})$, the elements $A_{mn\mu\nu}(k\overline{r})$ and $B_{mn\mu\nu}(k\overline{r})$ are changed to $RgA_{mn\mu\nu}(k\overline{r})$ and $RgB_{mn\mu\nu}(k\overline{r})$, respectively.

Subsequently, the excitation field equation for each scatterer is established individually to eventually form a full-rank matrix equation, represented as,

$$\overline{a}^{e} = \overline{a} + \overline{\overline{C}}\cdot\overline{a}^{e} \quad (22)$$

where

$$\overline{a}^{e} = \begin{bmatrix}\overline{a}^{e(1)}\\ \overline{a}^{e(2)}\\ \ldots\\ \overline{a}^{e(N_s)}\end{bmatrix} \quad (23)$$

$$\overline{a} = \begin{bmatrix}Rg\overline{\overline{\sigma}}(k\overline{r}_1)\cdot\overline{a}^{inc}\\ Rg\overline{\overline{\sigma}}(k\overline{r}_2)\cdot\overline{a}^{inc}\\ \ldots\\ Rg\overline{\overline{\sigma}}(k\overline{r}_{N_s})\cdot\overline{a}^{inc}\end{bmatrix} \quad (24)$$

$$\overline{\overline{C}} =$$

$$\begin{bmatrix}0 & \overline{\overline{\sigma}}(k\overline{r_1r_2})\cdot\overline{\overline{T}}^{(2)} & \ldots & \overline{\overline{\sigma}}(k\overline{r_1r_{N_s}})\cdot\overline{\overline{T}}^{(N_s)}\\ \overline{\overline{\sigma}}(k\overline{r_2r_1})\cdot\overline{\overline{T}}^{(1)} & 0 & \ldots & \overline{\overline{\sigma}}(k\overline{r_2r_{N_s}})\cdot\overline{\overline{T}}^{(N_s)}\\ \ldots & \ldots & \ldots & \ldots\\ \overline{\overline{\sigma}}(k\overline{r_{N_s}r_1})\cdot\overline{\overline{T}}^{(1)} & \overline{\overline{\sigma}}(k\overline{r_{N_s}r_2})\cdot\overline{\overline{T}}^{(2)} & \ldots & 0\end{bmatrix} \quad (25)$$

The excitation field coefficient $\overline{a}^{e}$ can be solved from Eq. (22) given the incidence field coefficient $\overline{a}$ and the T-matrix of the scatterers as discussed in Section 2. The scattering field coefficient can be subsequently calculated from Eq. (6) with the obtained $\overline{a}^{e}$, from which the total scattered field can be represented,

$$\overline{E}^{s}(\overline{r}) = \sum_{j=1}^{N_s}\Big\{\sum_{mn}a_{mn}^{s(M)(j)}\overline{M}_{mn}(k\overline{rr_j})$$

$$+a_{mn}^{s(N)(j)}\overline{N}_{mn}(k\overline{rr_j})\Big\} \quad (26)$$

while the total field can be calculated following Eq. (12).

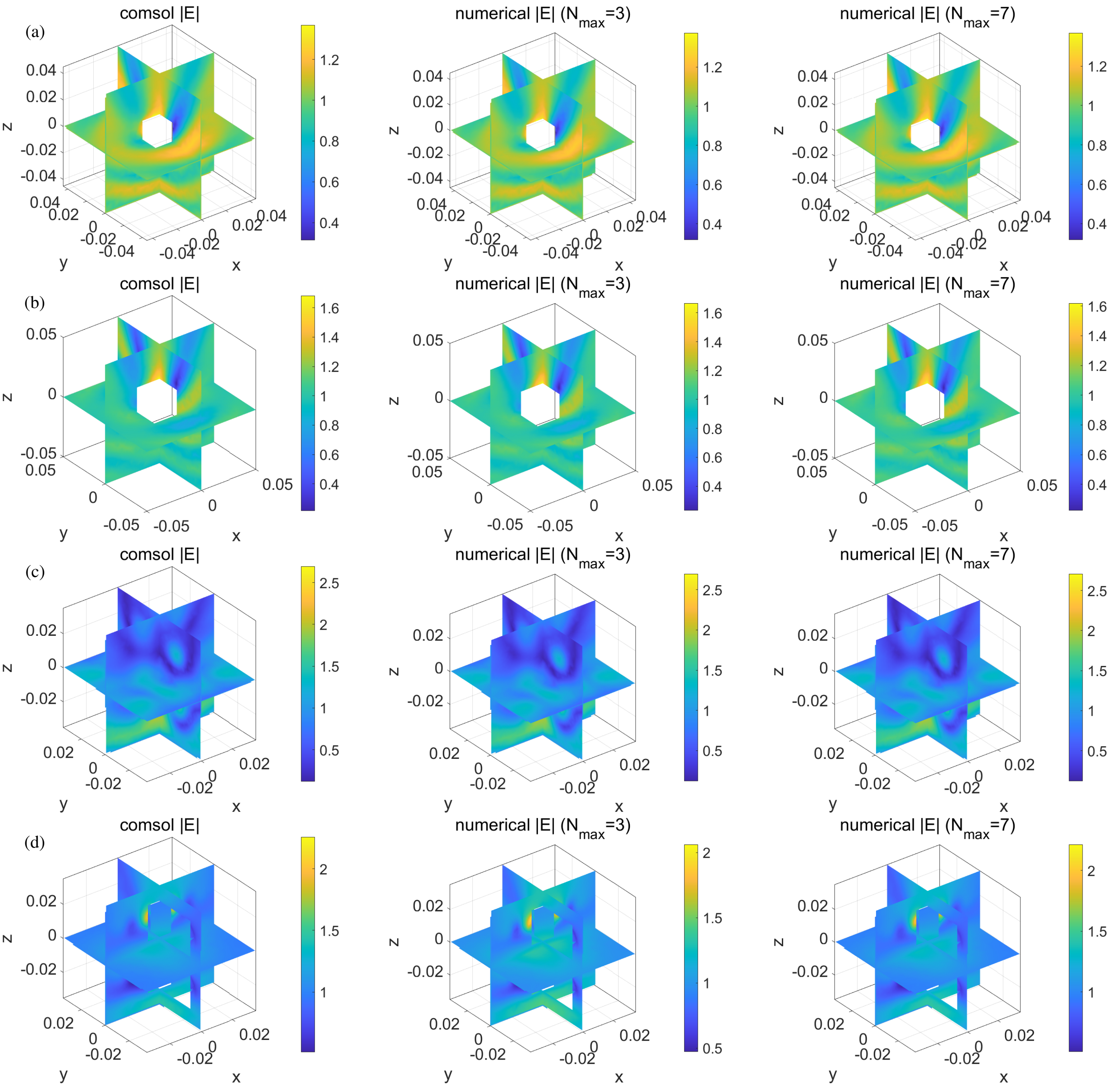

FIGURE 10. The total field was generated using a plane wave, $E_x = e^{ikz}$, and the outcomes were compared with those from COMSOL, employing a third-order and a seventh-order T-matrix for electric field reduction. The total field configurations for various geometries are presented: (a) a sphere of radius 0.01 m at the origin, (b) a cube with a side length of 0.02 m at the origin, (c) eight spheres of radius 0.01 m at $(\pm 0.015, \pm 0.015, \pm 0.015)$ m coordinates, and (d) eight complex structures at specific coordinates: $(0.01\sqrt{3}, 0.01, \pm 0.015)$, $(-0.01\sqrt{3}, 0.01, \pm 0.015)$, $(0, -0.02, \pm 0.015)$, $(0, 0, \pm 0.015)$ m.

It is noteworthy that the T-matrix of a scatterer is defined on a local reference frame of the scatterer and is relevant to its structure, composition, the background medium, and the wave frequency of interest, while independent to its position and orientation. In a multiple scattering problem, the T-matrix of individual scatterers can be precomputed and reused, while the change in the scatterer position and orientation is handled by the translation operator $\overline{\overline{\sigma}}$ through the addition theorem [39].

4.2. Numerical Validation of the Hybrid Multiple Scattering Theory

The effectiveness of the presented Foldy-Lax multiple scattering theory (MST) is verified in this subsection. Fig. 10 depicts the electric field in space for various scatterer configurations, as obtained using the hybrid Foldy-Lax MST and compared against those by the commercial COMSOL simulation software. Several scattering problems are tested,

TABLE 1. Comparison of computing time and number of unknowns in COMSOL and the proposed hybrid method for two multiple scattering examples.

		8 spheres	8 complex structures	215 complex structures
CPU Time	COMSOL Simulation	72 seconds	156 seconds	/
	Hybrid method ($N_{\max} = 3$)	2 seconds	2 seconds	49 seconds
	Hybrid method ($N_{\max} = 7$)	17 seconds	20 seconds	1,200 seconds
Number of Unknowns	COMSOL Simulation	1,896,222	7,538,540	188,985,482
	Hybrid method ($N_{\max} = 3$)	240	240	6,450
	Hybrid method ($N_{\max} = 7$)	1,008	1,008	27,090

encompassing both single and multiple scattering scenarios. Among them, Figs. 10(a) and (b) are single scattering problems with sphere and cube, respectively, positioned at the center of the coordinate. Fig. 10(c) is a multiple scattering problem with eight spheres located at coordinates $(\pm 0.015, \pm 0.015, \pm 0.015)$ m. Fig. 10(d) also involves multiple scattering, with eight complex structures positioned at the coordinates $(0.01\sqrt{3}, 0.01, \pm 0.015)$, $(-0.01\sqrt{3}, 0.01, \pm 0.015)$, $(0, -0.02, \pm 0.015)$, $(0, 0, \pm 0.015)$ m.

The results demonstrate that the electric field obtained through the proposed method exhibits a high degree of correlation with that obtained through COMSOL.

The relative errors compared to COMSOL results are within 1% at locations more than a quarter wavelength away from the scatterer when using up to the seventh-order T-matrix to obtain the electric field. In the context of multiple scattering, the proposed method exhibits enhanced time efficiency compared to COMSOL as the number of unknowns to be computed is significantly reduced. For example, in a scenario involving eight spheres and eight complex structures, COMSOL, utilizing multiple cores, requires 72 and 156 seconds, respectively, whereas the proposed method is particularly effective in improving the efficiency, with results obtained in approximately 2 seconds when only T-matrices up to the third order are used even with single-core computation. With T-matrix elements up to the seventh order, the method only requires 17 seconds and 20 seconds, respectively, in the two examples. The precise computing times and the number of unknowns involved are summarized in Table 1. Higher order T-matrix elements are needed to represent fields closer to the scatterer more accurately. When there are a large number of scatterers in the simulation scene, the advantages of the hybrid method become more pronounced. In COMSOL simulations, the involved unknowns not only on the number of scatterers but also on the size of the simulation domain. This means that when the scatterers are sparsely arranged, more memory will be required. In contrast, the number of unknowns in the hybrid method depends solely on the number of scatterers and is much smaller than that of full-wave methods, ensuring the feasibility of simulations with a large number of scatterers. Furthermore, if parallel computing is implemented in the hybrid method, the time advantage will be further amplified. In Fig. 11, we have added a multiple scattering scenario with 215 complex structures as described before arranged in a $6 \times 6 \times 6$ array with a 20 mm spacing, centered at the origin. The complex structure centered at $(-30, -30, -30)$ mm was replaced with a Hertzian dipole with a dipole moment of 10^{-5} $\mathrm{A \cdot m}$ in $\hat{z}$-direction. The simulation took 49 seconds, with 6,450 unknowns using the proposed hybrid approach. A similar simulation in COMSOL would involve 188,985,482 unknowns which consumes approximately 1 TB of memory and requires advanced computing facility to handle. Note the reported computing time for the hybrid MST method does not include the time to extract the T-matrix, which is a one-time overhead for each scatterer category at the given frequency of interest. In our current implementation combing COMSOL and Matlab for the T-matrix extraction, it takes about 7 hours to compute the T-matrix elements of complex structure up to 7 orders, while 2 hours up to 5 orders and half an hour up to 3 orders.

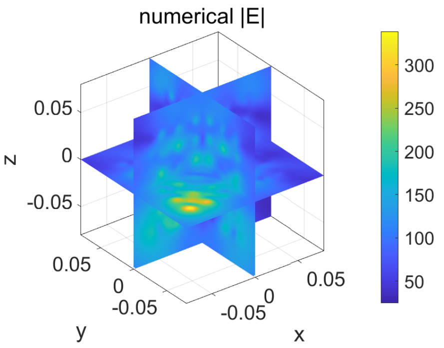

FIGURE 11. The electric field obtained from a periodic array of 215 complex structures under a Hertzian dipole excitation.

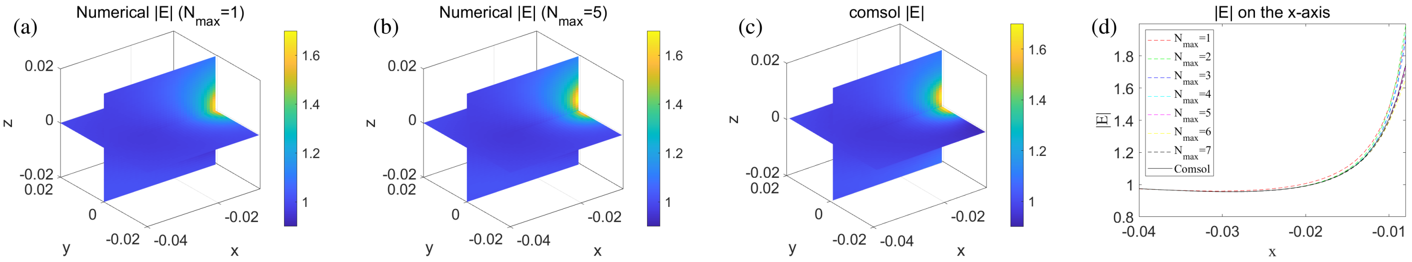

FIGURE 12. Convergence of electric fields obtained using the T-matrix method. (a), (b) The electric field obtained using the T-matrix of $N_{\max} = 1, 5$ separately. (c) Electric field obtained using COMSOL simulation. (d) Modulus of the total field on the x-axis for different $N_{\max}$ T-matrices.

Figure 12 illustrates the convergence of the electric field calculated using the T-matrix method, which placing a complex structure at the point of origin using plane wave $E_x = e^{ikz}$ of 5 GHz as an incident wave. By observing the variation of the modulus of the field on the x-axis obtained from the T-matrices with different $N_{\max}$ in Fig. 12(d), we can find that the electric field converges with $N_{\max} = 1$ in the far region from the scatterer, consistent with the results from COMSOL. However, closer to the scatterer, specifically near the effective area threshold, the T-matrix requires $N_{\max} = 5$ to match the COMSOL simulation results. This confirms that the scattering field converges more quickly in the far region using spherical wave expansions, while higher order spherical wave coefficients are needed in the near region to accurately represent the accurate electric field distribution.

5. CONCLUSIONS

This paper introduces a new hybrid approach that combines spherical wave expansion and full-wave simulation to extract the T-matrix of arbitrary-shaped scatterers. It also explores the use of spherical waves for representing incident fields from arbitrary sources. The study then integrates the Foldy-Lax multiple scattering theory with the extracted T-matrix to analyze electromagnetic scattering in scenarios involving multiple arbitrarily shaped scatterers. The effectiveness of the proposed T-matrix extraction technique is demonstrated through several numerical examples, revealing its dependency on the distance of the enclosing surface from the scatterer, particularly in higher-order components. The accuracy of the electric field obtained from a point source using spherical waves is influenced by the distance from the source and the order of spherical waves utilized. Similarly, when utilizing the T-matrix to reconstruct the electric field, accuracy is linked to the distance from the scatterer and its shape. The research findings indicate that the hybrid method efficiently combines the advantages of the full-wave method in modeling arbitrary individual scatterers with the analytical approach based on wave expansion, yielding a feasible representation of the individual scattering characteristics through its low-order T-matrix. Furthermore, the combination of the T-matrix extraction technique and the Foldy-Lax MST effectively addresses multiple scattering challenges in complex structures, and it also offers a practical solution for modeling arbitrary incident fields with numerically derived coefficients. Moreover, the T-matrix elements and the excitation field coefficients are noted to be smooth with frequency, indicating their applications in broadband simulations through interpolations. The proposed hybrid method significantly enhances computational efficiency by about an order of magnitude through significantly reducing the degree of freedoms in representing the complicated scattering behaviors of each scatterer when compared to traditional full-wave simulations, enabling rapid simulation of intricate electromagnetic structures in various engineering applications.

ACKNOWLEDGEMENT

This work was supported by the National Key Research and Development Program of China under Grant 2022YFB3903300 and Grant 2022YFB3903304. It was also supported by the National Natural Science Foundation of China (61901411) and the startup funds of Zhejiang University. Haifeng Zheng and Xuyang Bai are co-first authors that contributed equally to this work. This work was led by principal investigator and corresponding author Shurun Tan.

REFERENCES

[1] Wang, H., S. K. Gupta, B. Xie, and M. Lu, "Topological photonic crystals: A review," *Frontiers of Optoelectronics*, Vol. 13, 50–72, 2020.

[2] Xia, L., Y. Feng, and B. Zhao, "Intrinsic mechanism and multiphysics analysis of electromagnetic wave absorbing materials: New horizons and breakthrough," *Journal of Materials Science & Technology*, Vol. 130, 136–156, 2022.

[3] Bai, X., R. Li, S. Tan, S. Mikki, and E. Li, "An electromagnetic analysis of the impact of random scattering and RISs on the shannon capacity of MIMO communication systems," *IEEE Antennas and Wireless Propagation Letters*, Vol. 23, No. 4, 1176–1180, 2023.

[4] Li, R., D. Li, J. Ma, Z. Feng, L. Zhang, S. Tan, W. E. I. Sha, H. Chen, and E.-P. Li, "An electromagnetic information theory based model for efficient characterization of MIMO systems in complex space," *IEEE Transactions on Antennas and Propagation*, Vol. 71, No. 4, 3497–3508, 2023.

[5] Huang, S. and L. Tsang, "Fast broadband modeling of traces connecting vias in printed circuit boards using broadband Green's function method," *IEEE Transactions on Components, Packaging and Manufacturing Technology*, Vol. 7, No. 8, 1343–1355, 2017.

[6] Chang, X. and L. Tsang, "Fast and broadband modeling method for multiple vias with irregular antipad in arbitrarily shaped power/ground planes in 3-D IC and packaging based on general-

ized Foldy-Lax equations," *IEEE Transactions on Components, Packaging and Manufacturing Technology*, Vol. 4, No. 4, 685–696, 2014.

[7] Xu, R., R. Li, D. Li, and E.-P. Li, "Electromagnetic analysis in PINMAP assignment optimization based on T-matrix method," in *2022 IEEE 22nd International Conference on Communication Technology (ICCT)*, 99–103, Nanjing, China, 2022.

[8] Wu, Y. M. and W. C. Chew, "The modern high frequency methods for solving electromagnetic scattering problems," *Progress In Electromagnetics Research*, Vol. 156, 63–82, 2016.

[9] Wang, C.-F., C. Y. Kee, and Z.-L. Liu, "Development of hybrid high frequency simulation tool for rapid modeling of electromagnetic scattering from large and complex structures," in *2016 IEEE International Conference on Computational Electromagnetics (ICCEM)*, 98–100, Guangzhou, China, 2016.

[10] Silvester, P. P. and R. L. Ferrari, *Finite Elements for Electrical Engineers*, 3rd ed., Cambridge University Press, 1996.

[11] Jin, J.-M., *The Finite Element Method in Electromagnetics*, 3rd ed., John Wiley & Sons, 2015.

[12] Kunz, K. S. and R. J. Luebbers, *The Finite Difference Time Domain Method for Electromagnetics*, 1st ed., CRC Press, 1993.

[13] Taflove, A., S. C. Hagness, and M. Piket-May, "Computational electromagnetics: The finite-difference time-domain method," *The Electrical Engineering Handbook*, Vol. 3, 629–670, 2005.

[14] Harrington, R. F. and J. L. Harrington, *Field Computation by Moment Methods*, Oxford University Press, 1996.

[15] Gemmer, T. M. and D. Heberling, "Accurate and efficient computation of antenna measurements via spherical wave expansion," *IEEE Transactions on Antennas and Propagation*, Vol. 68, No. 12, 8266–8269, 2020.

[16] Alian, M. and N. Noori, "A domain decomposition method for the analysis of mutual interactions between antenna and arbitrary scatterer using generalized scattering matrix and translation addition theorem of SWFs," *IEEE Transactions on Antennas and Propagation*, Vol. 71, No. 10, 8088–8096, 2023.

[17] Jeong, J., L. Tsang, W. Gu, A. Colliander, and S. H. Yueh, "Wave propagation in vegetation field by combining fast multiple scattering theory and numerical electromagnetics in a hybrid method," *IEEE Transactions on Antennas and Propagation*, Vol. 71, No. 4, 3598–3610, 2023.

[18] Schulz, F. M., K. Stamnes, and J. J. Stamnes, "Scattering of electromagnetic waves by spheroidal particles: A novel approach exploiting the T matrix computed in spheroidal coordinates," *Applied Optics*, Vol. 37, No. 33, 7875–7896, 1998.

[19] Waterman, P. C., "Matrix formulation of electromagnetic scattering," *Proceedings of the IEEE*, Vol. 53, No. 8, 805–812, 1965.

[20] Nieminen, T. A., H. Rubinsztein-Dunlop, and N. R. Heckenberg, "Calculation of the T-matrix: General considerations and application of the point-matching method," *Journal of Quantitative Spectroscopy and Radiative Transfer*, Vol. 79, 1019–1029, 2003.

[21] Farafonov, V. G., A. A. Vinokurov, and V. B. Il'in, "Comparison of the light scattering methods using the spherical basis," *Optics and Spectroscopy*, Vol. 102, 927–938, 2007.

[22] Hu, M. and G. Xiao, "Compressed T-matrix for arbitrarily shaped objects," in *2024 IEEE International Symposium on Antennas and Propagation and INC/USNC-URSI Radio Science Meeting (AP-S/INC-USNC-URSI)*, 1337–1338, Firenze, Italy, 2024.

[23] Xiao, G. and J.-F. Mao, "Generalized transition matrix for arbitrarily shaped scatterers with composite structures," *IEEE Transactions on Electromagnetic Compatibility*, Vol. 51, No. 2, 401–405, 2009.

[24] Tsang, L., T.-H. Liao, R. Gao, H. Xu, W. Gu, and J. Zhu, "Theory of microwave remote sensing of vegetation effects, SoOp and rough soil surface backscattering," *Remote Sensing*, Vol. 14, No. 15, 3640, 2022.

[25] Kim, K. T. and B. A. Kramer, "Direct determination of the T-matrix from a MoM impedance matrix computed using the Rao-Wilton-Glisson basis function," *IEEE Transactions on Antennas and Propagation*, Vol. 61, No. 10, 5324–5327, 2013.

[26] Rubio, J., J. R. Mosig, R. Gómez-Alcalá, and M. A. G. de Aza, "Scattering by arbitrary cross-section cylinders based on the T-matrix approach and cylindrical to plane waves transformation," *IEEE Transactions on Antennas and Propagation*, Vol. 70, No. 8, 6983–6991, 2022.

[27] Ozawa, T., H. M. Price, A. Amo, N. Goldman, M. Hafezi, L. Lu, M. C. Rechtsman, D. Schuster, J. Simon, O. Zilberberg, and I. Carusotto, "Topological photonics," *Reviews of Modern Physics*, Vol. 91, No. 1, 015006, 2019.

[28] Kim, M., Z. Jacob, and J. Rho, "Recent advances in 2D, 3D and higher-order topological photonics," *Light: Science & Applications*, Vol. 9, No. 1, 130, 2020.

[29] Mooshammer, F., M. A. Huber, F. Sandner, M. Plankl, M. Zizlsperger, and R. Huber, "Quantifying nanoscale electromagnetic fields in near-field microscopy by Fourier demodulation analysis," *ACS Photonics*, Vol. 7, No. 2, 344–351, 2020.

[30] Zhi, K., C. Pan, H. Ren, K. K. Chai, C.-X. Wang, R. Schober, and X. You, "Performance analysis and low-complexity design for XL-MIMO with near-field spatial non-stationarities," *IEEE Journal on Selected Areas in Communications*, Vol. 42, No. 6, 1656–1672, 2024.

[31] Mikki, S., "Theory of nonsinusoidal small antennas for near-field communication system analysis," *Progress In Electromagnetics Research B*, Vol. 86, 177–193, 2020.

[32] Gu, W., L. Tsang, A. Colliander, and S. H. Yueh, "Wave propagation in vegetation field using a hybrid method," *IEEE Transactions on Antennas and Propagation*, Vol. 69, No. 10, 6752–6761, 2021.

[33] Tsang, L., J. A. Kong, and K.-H. Ding, *Scattering of Electromagnetic Waves: Theories and Applications*, John Wiley & Sons, 2000.

[34] Frei, W., "Simulation tools for solving wave electromagnetics problems," Available: https://www.comsol.com/blogs/simulation-tools-for-solving-wave-electromagnetics-problems, 2015.

[35] Griesmer, F., "Using matlab® functions in your comsol multiphysics® models," Available: https://www.comsol.com/blogs/using-matlab-functions-comsol-multiphysics-models, 2014.

[36] Cruzan, O. R., "Translational addition theorems for spherical vector wave functions," *Quarterly of Applied Mathematics*, Vol. 20, No. 1, 33–40, 1962.

[37] Tai, C.-T., *Dyadic Green's Functions in Electromagnetic Theory*, 1st ed., Intext Educational Publishers, 1971.

[38] Tsang, L., J. A. Kong, K.-H. Ding, and C. O. Ao, *Scattering of Electromagnetic Waves: Numerical Simulations*, 533–540, John Wiley & Sons, 2004.

[39] Khajeahsani, M. S., F. Mohajeri, and H. Abiri, "Rotational vector addition theorem and its effect on T-matrix," *IEEE Transactions on Antennas and Propagation*, Vol. 59, No. 10, 3819–3825, 2011.